$SrTa_2O_6$ thin films for high-*K* dielectric applications grown by chemical vapor deposition on different substrates

Stephan Regnery
Institut für Festkörperforschung and Center of Nanoelectronic Systems for Information Technology, Forschungszentrum Jülich, D-52425 Jülich, Germany
and AIXTRON AG, Kackertstr. 15-17, D-52072 Aachen, Germany

Reji Thomas, Peter Ehrhart,[a] and Rainer Waser
Institut für Festkörperforschung and Center of Nanoelectronic Systems for Information Technology, Forschungszentrum Jülich, D-52425 Jülich, Germany

(Received 26 August 2004; accepted 26 January 2005; published online 28 March 2005)

$SrTa_2O_6$ thin films with thickness between 6 and 150 nm were deposited by metal-organic chemical vapor deposition in a multiwafer planetary reactor. The monomolecular precursor, strontium-tantalum-(methoxyethoxy)-ethoxide, was dissolved in toluene and injected by a liquid delivery system. A rather narrow process window for the deposition of stoichiometric $SrTa_2O_6$ was found for this precursor at low pressures and a susceptor temperature around 500 °C. Films were grown on $Pt/TiO_2/SiO_2/Si$, TiN_x/Si, and SiO_2/Si substrates. The as-deposited films were x-ray amorphous and could be crystallized by postannealing at a temperature $\geqslant$700 °C. The distorted tetragonal tungsten bronze phase of $SrTa_2O_6$ was dominating within a broad range of compositions (Sr/Ta: 0.4–0.7) and a perovskite-type phase was additionally observed for $Sr/Ta > 0.7$ and predominated for $Sr/Ta > 1$. The electrical properties have been investigated with metal-insulator-metal and metal-insulator-semiconductor capacitors after sputter deposition of Pt top electrodes. The amorphous films had a dielectric constant *K* in the range of 35–45 and low leakage currents. For stoichiometric $SrTa_2O_6$ the dielectric permittivity reached values of $K = 100$–110, but the leakage currents were increased. Remarkably, the permittivity is not very sensitive to deviations from the exact stoichiometry of the $SrTa_2O_6$ phase (Sr/Ta: 0.4–0.7), but a decrease to values of $K = 30$–40 is observed along with the transition to the perovskite phase at high Sr contents. © *2005 American Institute of Physics*. [DOI: 10.1063/1.1873033]

I. INTRODUCTION

Along with the ongoing miniaturization of electronic devices high-*K* thin films are needed for a very broad application area, including capacitor dielectrics for future dynamic random access memories (DRAMs), embedded capacitors, tunable devices, as well as gate oxides for field effect transistors.[1] The spectrum of materials has been reviewed recently[2] and includes medium-*K* binary oxides like ZrO_2, HfO_2, and Ta_2O_5 with a dielectric constant *K* between 20 and 40, as well as crystalline perovskites, especially the $[Ba_xSr_{(1-x)}]TiO_3$ solid solution series, which reach values of several hundreds Recently, $SrTa_2O_6$ (STA) has been discussed in addition, as it has promising properties in amorphous form ($K \approx 40$) as well as in crystalline form ($K \approx 100$).[3] Different phases of STA, which contain perovskite-like building blocks, are known for some time, but the processing of ceramics needs high temperatures and quite complicated processing strategies.[4] However, along with the development of chemical deposition methods for thin films of ferroelectric $SrBi_2Ta_2O_9$, precursors became available, which allow for a straightforward deposition of STA thin films by chemical solution deposition (CSD),[4–6] metal-organic chemical vapor deposition (MOCVD),[7,8] and atomic layer deposition (ALD).[3,9,10] Films have been deposited on Pt/Si by CSD,[4] MOCVD,[8] and ALD (Ref. 3) and on $SiO_x/Si(100)$ by CSD,[5,6] MOCVD,[7,8] and ALD.[9,10] Considering the dependence of the electrical properties of the films on stoichiometry and annealing temperature, the results obtained after deposition by the different chemical methods on Pt/Si seem very consistent.[3,4,8] For the films grown on Si the interfacial layer of SiO_x is important and reduces the effective dielectric constant dependent on the film thickness,[5,9] this interfacial layer growth can be reduced by an oxygen diffusion barrier of oxinitride, SiON.[5,6] Nevertheless, an astonishing high capacity, as characterized by the equivalent oxide thickness (EOT) of a capacitor with a SiO_2 dielectric, of ~1 nm has been reported for 5-nm thick STA layers independent of the interlayer.[6]

We report on MOCVD of STA thin films within a wide range of compositions including different crystalline phases. Depositions are performed under identical conditions on different substrates $Pt/TiO_2/SiO_x/Si$ and TiN_x/Si, which yield test structures for capacitor applications, i.e., metal-insulator-metal (MIM) structures, as well as on $SiO_x/Si(100)$, which yield test structures for gate oxide application, i.e., metal-insulator-silicon (MIS) structures. The electrical properties of the MIM and MIS structures were deduced from the *C–V* and *I–V* characteristics. As the electrical properties of thin

[a]Electronic mail: p.ehrhart@fz-juelich.de

TABLE I. Standard MOCVD process parameters.

Susceptor temperature	500 °C
Process pressure	2.0 mbar
Averaged precursor flow rate	0.6 ml/min
Oxygen flow rate	500 SCCM (standard cubic centimeter per minute)
Ar-carrier flow rate	1300 SCCM
Growth rate	8–10 nm/min

films such as permittivity and leakage current may depend on film thickness, the final discussion is based on different thickness series.

II. EXPERIMENTAL DETAILS

$SrTa_2O_6$ films were deposited in an AIXTRON 2600G3 Planetary Reactor®, which can handle five 6-in. wafers simultaneously. This reactor is characterized by a central gas inlet, which makes this reactor a radial flow system.[11] We used a monomolecular precursor, strontium-tantalum-(methoxyethoxy)-ethoxide $Sr[Ta(OC_2H_5)_5(OC_2H_4OCH_3)]_2$, which was dissolved in toluene in a 0.05-molar solution. This precursor solution was injected by a TRIJET system with a typical pulse length of 0.8 ms (corresponding to 0.005 ml of precursor solution) and with pulse distances of 0.5 s. This corresponds to an average precursor flow rate of 0.6 ml/min.

The main process parameters are summarized in Table I. The temperature of the wafer surface can be assumed to be 20–50 °C lower than the directly measured susceptor temperature for platinized substrates and additional for 20 °C lower for TiN_x/Si and Si substrates. The $Pt/TiO_2/SiO_x/Si$ substrates with a platinum thickness of l00 nm were preannealed at 600 °C in order to stabilize the grain structure. The TiN_x electrodes had a thickness of ~80 nm and the *p*-type Si(100) substrates were used without removing the native oxide layer of l–2 nm.

The stoichiometry and areal mass density of the deposited films were routinely determined by wavelength dispersive x-ray fluorescence spectroscopy (XRF) using calibration standards deposited by CSD. In order to deduce the film thickness in addition, the bulk density, $\rho = 7.6\ g/cm^3$ for $SrTa_2O_6$ was used. Hence, this thickness corresponds to the equivalent thickness of a $SrTa_2O_6$ layer with the bulk density and presents a lower limit for the film thickness, as the density of the films is generally lower than the bulk value. For strongly off-stoichiometric films the corresponding values for the mixed oxide of SrO ($\rho = 5.01\ g/cm^3$) and Ta_2O_5 ($\rho = 8.5\ g/cm^3$) were applied. Direct determinations of thickness and density were additionally performed by x-ray reflectivity (XRR).[12] The crystalline films reached the bulk density and the amorphous films also had a remarkably high density, which was only ~5% below the bulk values. Therefore, the XRF values were applied in the following without further corrections. The phase determination of the films was carried out in a Philips MRD x-ray diffractometer, using Cu $K\alpha$ radiation and a diffracted beam monochromator. Generally, the glancing incidence geometry with an angle of incidence of 2° was applied.

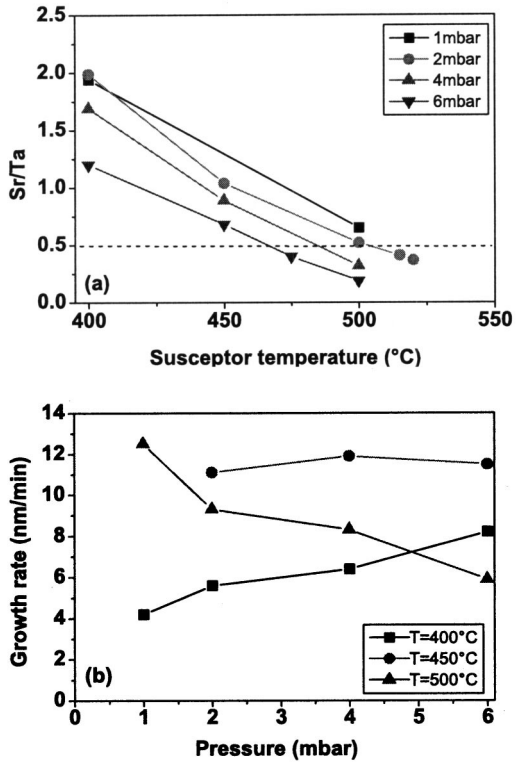

FIG. 1. Film stoichiometry, Sr/Ta, and growth rate as a function of the susceptor temperature and the reactor pressure, (a) Sr/Ta vs deposition temperature for different pressures as indicated in the inset. A narrow process window is obtained for stoichiometric films, e.g., a pressure of 2 mbar at 500 °C and a pressure of 6 mbar at ~470 °C; (b) growth rate vs pressure for the deposition temperatures given in the inset. A different pressure dependence is observed for different T_{dep}.

For electrical measurements, Pt electrode pads were sputter-deposited on top of the STA films and patterned using shadow masks or lift-off lithography providing areas of 0.050, 0.018, and 0.011 mm^2. For the MIS structures a GaIn eutectic paste was applied manually to make an ohmic backside contact. The resulting film stack was Pt/STA/*p*-Si/$Ga_{0.85}In_{0.15}$. Capacitance–voltage curves were obtained with a HP #4284 LCR meter using a frequency of 100 kHz. Leakage currents were measured using a Burster 4462 voltage generator and a Keithley 617 electrometer with a detection limit of 50 fA. *I–V* curves were generated by a stepwise increase of the voltage and the current data were taken after a holding time of 30 s after the voltage steps.

III. FILM GROWTH

In spite of the use of a stoichiometric monomolecular precursor there was only a very narrow process window for the deposition of stoichiometric films in the temperature–pressure parameter field. Figure 1(a) shows the dependence of the Sr/Ta ratio on the susceptor temperatures for different reactor pressures. We observe a decrease of the ratio with increasing temperature for all pressures. We obtain the stoichiometric composition at 500 and 470 °C for depositions with 2 and 6 mbar, respectively. Figure 1(b) shows the pressure dependence of the growth rate and we observe a different behavior for different deposition temperatures. The de-

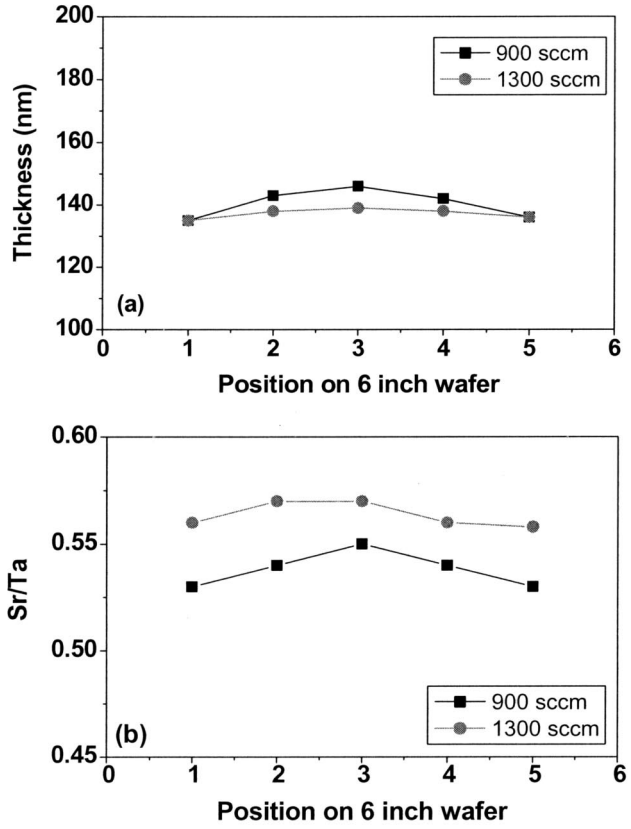

FIG. 2. Homogeneity of the films across a 6-in. wafer as determined by XRF on 1×1-in.^{2} pieces cut along a wafer diameter. (a) Thickness and (b) stoichiometry.

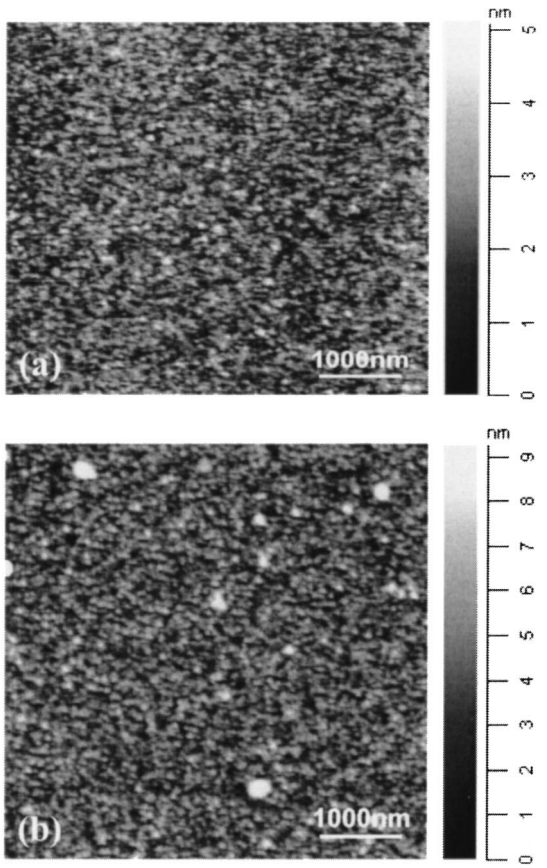

FIG. 3. AFM images of the surface structure of STA films of ~80 nm thickness: (a) Deposition on TiN_x/Si and (b) on Pt/TiO_x/SiO_x/Si. The rms roughness is 0.75, and 1.55 nm, respectively (remind different scale for the images).

crease of the growth rate with increasing pressure observed at 500 °C indicates the influence of gas-phase reactions. The increase observed at low pressures is a consequence of the pulsed precursor injection as observed also with depositions of HfO_2 (Ref. 13). At low T_{dep} the reaction speed is limited and is too slow at the peak of the injection pulse; hence, the lower gas speed and the related longer residence time at higher pressures increases the growth rate. At the intermediate temperature of 450 °C the growth rate is rather stable, however, stoichiometry is not achieved. In spite of the different processing conditions the observed narrow window for stoichiometric films is similar to earlier MOCVD depositions with two different monomolecular precursors.[7] We selected a low pressure of 2 mbar for the standard deposition as the performance was more stable at this pressure and the efficiency of the precursor incorporation into the film, which is for identical precursor flow rates directly related to growth rate, was slightly higher than for 6 mbar and reached a value of ~30%.

Although there is a narrow process window, a very good homogeneity of the films in thickness as well as in stoichiometry could be achieved by adjusting the gas flow rate. The variation of thickness and stoichiometry was determined by XRF on 1×1 in.^{2} parts of the wafer along a diameter of a 6-in. wafer and is shown in Fig. 2. Along with this optimization of the homogeneity, the absolute value of the stoichiometry shifted slightly and had to be adjusted by a small increase of the deposition temperature. The standard deviation was 1.2% in thickness and 0.9% in the Sr/Ta ratio for the given slightly Sr-rich film of 135 nm thickness.

IV. FILM STRUCTURE AND MORPHOLOGY

Films deposited at $T\sim500$ °C were x-ray amorphous on all substrates. Figure 3 shows that the films had a very low roughness as determined by atomic force microscopy (AFM), e.g., the root-mean-square (rms) variation of the roughness were 0.8 and l.6 nm for ~80-nm thick films on TiN_x and Pt bottom electrodes, respectively. The higher roughness of Pt might be related to the higher roughness of the Pt bottom electrode.

The amorphous structure was stable up to 600 °C and crystallization was observed after annealing for typically 30 min at $T>700$ °C, as shown in Fig. 4(a). Similar results were obtained for all substrates, and independent of the atmosphere, N_2 or O_2. The crystalline structure agrees with the structure of $SrTa_2O_6$ reported in the literature[14] and can be described as an orthorhombic distorted tetragonal tungsten bronze structure. Figure 4(b) shows the changes of the structure for different stoichiometry. It should be mentioned that the Pt-(111) and Pt-(200) reflections are sometimes visible at ~40° and ~46°, respectively, although they would be completely suppressed in the present glancing incidence geometry for a really perfect (111)-texture. This indicates some

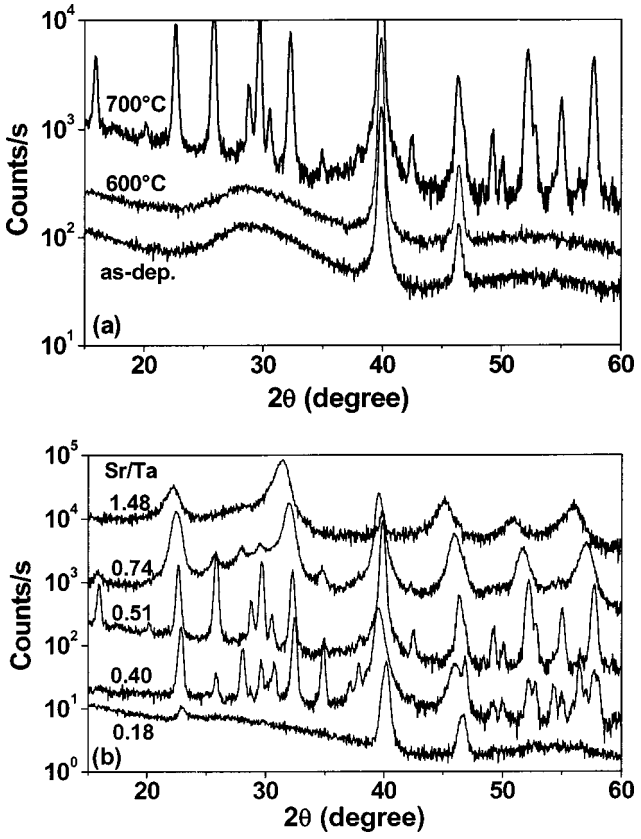

FIG. 4. Phase evolution during thermal annealing. (a) Stoichiometric film of 78-nm thickness; the peaks at ~40° and ~46° correspond to the Pt electrode. (b) Stoichiometry dependence of the structure observed after annealing at 800 °C.

variance in the quality of the presently used substrates. Within a rather broad range around ideal stoichiometry, Sr/Ta=0.4–0.6, the orthorhombic structure seems predominant. For larger values we observe first a mixed phase and finally, for the example of Sr/Ta=1.48, a new phase with rather broad reflections. This pattern resembles exactly a cubic perovskite as first observed by Rodriguez *et al.*[4] however, the line broadening indicates high defect densities and might include planar defects like stacking faults and antiphase boundaries in addition to cation vacancies as discussed earlier.[4] For very low Sr content (Sr/Ta~0.18) Fig. 4(b) indicates some Ta_2O_5 precipitates in a seemingly amorphous matrix.

Although there is a similar phase evolution for films deposited on TiN_x electrodes, the TiN_x is not stable during annealing at $T>550$ °C and is oxidized into the insulating rutile phase of TiO_2, as demonstrated in Fig. 5. Hence, these capacitors are destroyed and electrical data are obtained only for amorphous films.

For the Si(100) substrates we observe again the same phase evolution; however, major interfacial reactions are observed along with the crystallization, which deteriorate the MIS properties. This reaction is evidenced by XRR, as shown in Fig. 6. Similar to observations with the films on Pt we observe for thick films, >15 nm, a small increase of the critical angle for total reflection, which corresponds to an increase of the density by ~5% along with the crystallization, and consistently the period of the thickness oscillations,

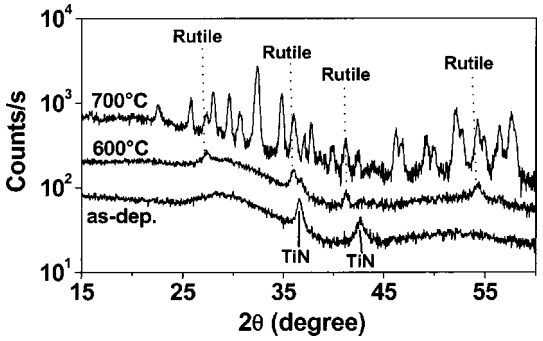

FIG. 5. Annealing of STA on TiN_x. The TiN_x is oxidized to rutile at temperatures lower than the crystallization temperature of the STA.

which is directly related to the film thickness $t\sim 1\Delta/\vartheta$ increases. For very thin films, <15 nm, we observe, however, the opposite behavior, as shown in Fig. 6, which indicates strong interdiffusion reactions with the Si substrate.

V. ELECTRICAL PROPERTIES

A. Pt/STA/Pt MIM capacitor structures

Typical *C–V* characteristics for Pt/STA/Pt capacitors are shown in Fig. 7. For the amorphous STA we observe a rather constant capacity, i.e., a variation of <0.1% within the voltage range of 0 to 6 V and a low and also nearly constant loss angle of tan $\delta\sim 0.001$. After crystallization there is an increase of the capacity by a factor of ~3 and the voltage dependence increases to ~2%. This field dependence is remarkably small as compared to known high-*K* materials with perovskite structure. In addition, the dielectric loss increases from tan $\delta\sim 0.001$ to 0.01 after crystallization.

Figure 8 summarizes the stoichiometry dependence of the dielectric constant *K*. For the amorphous films we observe a value of 35±5 with no significant change within the wide range of composition. There is, however, a significant increase in the loss angle for Ta-rich films (Sr/Ta<0.4). After annealing we observe an increase of the dielectric constant to values around 100 within a range of Sr/Ta=0.4–0.6, where the orthorhombic structure is dominant. However, this increased *K* is correlated with an increased loss angle. Remarkably, there is no increase for the perovskite phase, which is in agreement with the low value of 16 reported

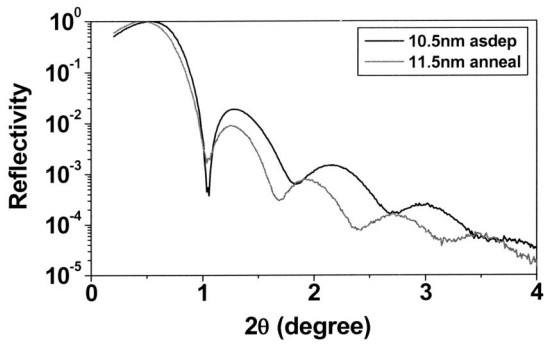

FIG. 6. XRR curve for a ~11-nm thin STA film on Si and of the changes after crystallization.

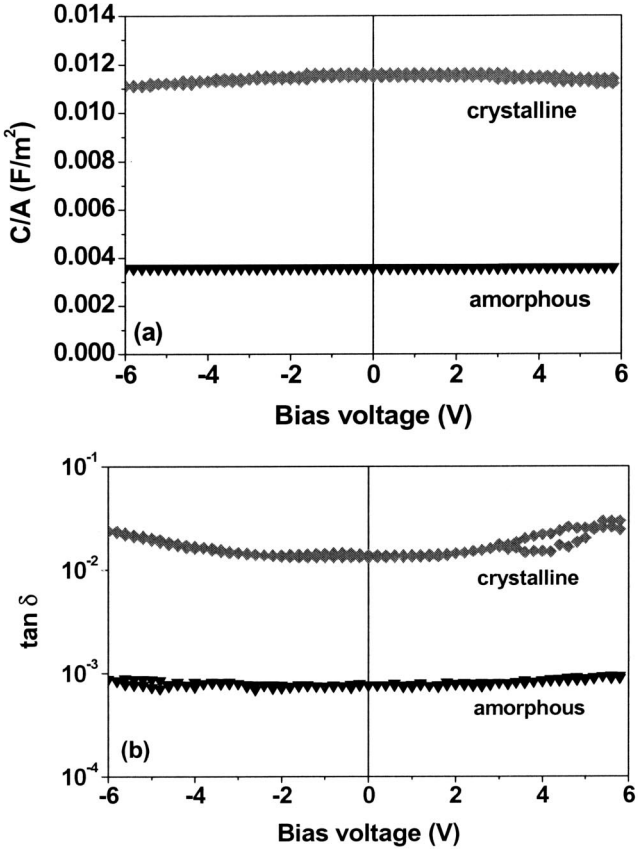

FIG. 7. *C–V* characteristics (a) and loss tangent (b) for a 78-nm STA film. Data are shown for the as-deposited, amorphous state, and the crystalline state as obtained after annealing at 700 °C.

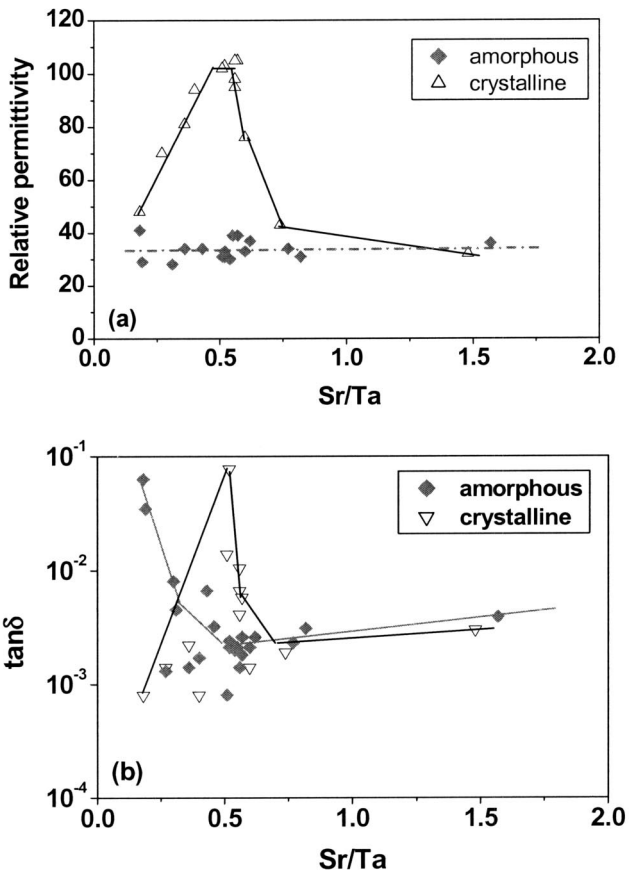

FIG. 8. Stoichiometry dependence of the permittivity (a) and the loss tangent (b) for amorphous and crystalline STA films of 50–80 nm thickness.

earlier for this phase.[4] The broad maximum indicates that an exact stoichiometry control is not necessary for the application of STA dielectric films.

Figure 9 summarizes the thickness dependence of K in a plot of the reciprocal capacity versus thickness. For the amorphous films there is a larger scatter of the data and a linear regression yields a small negative offset; therefore, the fit was forced through the origin. The slope of the line yields an average bulk value of $K=33\pm1.5$ consistent with the effective $K\sim35$ given above. For the crystalline films the slope of an unforced linear fit yields an average K value of 110 ± 11. The offset at zero indicates an interfacial capacity, "dead layer." $\mathrm{EOT}_{\mathrm{interface}}\sim0.27\pm0.3$ nm. This value is similar to those observed for $SrTiO_3$ films on Pt electrodes. This extrapolation contains a larger uncertainty and data for thinner films would be necessary, however, thin crystalline films were more leaky.

For the amorphous films the leakage is very low, i.e, at the limit of the experimental resolution (10^{-10} A/cm^2), up to fields of 1500 kV/cm, as shown in Fig. 10 for the example of a 48-nm thick amorphous film. There is no degradation up to fields of 2500 kV/cm as demonstrated by the coincidence of three recording loops. After crystallization the leakage currents are drastically increased and, as demonstrated for a 30-nm thick crystalline film, there seems to be some relaxation during the first loop, but reasonable reproducibility later on. In addition, the leakage curves for crystalline films are very asymmetric even for the Pt/STA/Pt structure. We attribute this irregular behavior largely to the grain growth and recrystallization of the Pt bottom electrodes during annealing at 700–800 °C, which is much higher than the predeposition anneal at 600 °C. This may introduce grain boundary segregation and also some cracks, which cause leakage for the thinnest films.

The leakage currents averaged for positive and negative bias are presented in a Schottky plot for amorphous and crystalline films of different thicknesses in Fig. 11. For the nearly stoichiometric amorphous films we observe leakage currents below 10^{-9} A/cm^2 up to fields of $\sim$2000 kV/cm, indepen-

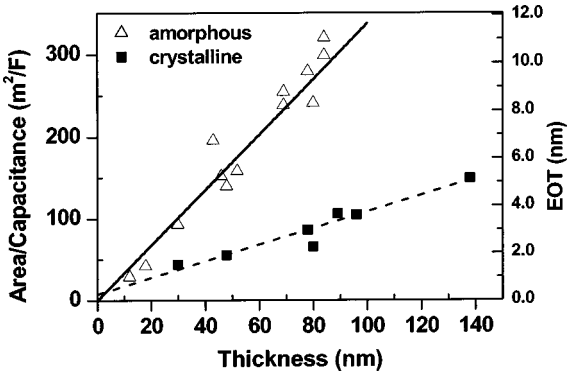

FIG. 9. Reciprocal capacity vs film thickness for Pt/STA/Pt capacitors. The corresponding EOT is given at the left ordinate.

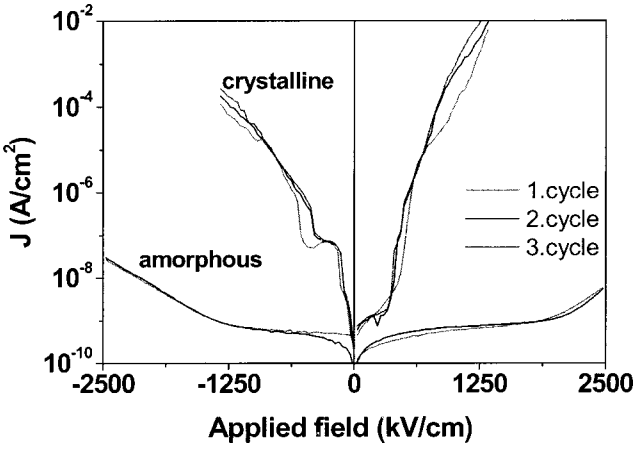

FIG. 10. Leakage current for amorphous and crystalline STA on Pt electrodes. Examples are given for a 48-nm thick amorphous film and a 30-nm thick crystalline film. Small variations are observed for succeeding measuring cycles of the crystalline film.

dent of the film thickness. Only for very far-off stoichiometry, Sr/Ta=0.18 and 1.57, respectively, do we observe a significant increase of the leakage currents. Within the low-field region the currents are at the limit of the experimental resolution and do not allow for a detailed analysis of the slope and a discussion of the underlying leakage mechanism. In addition, the leakages at low fields may be affected by a slow relaxation at room temperature and thus represent upper limits for the leakage. This behavior is indicated in Fig. 12, which additionally shows the beginning of degradation at fields larger than ~3 MV/cm. Nevertheless, the comparison to the data on TiN electrodes, discussed below, indicates a major influence of the electrode on the leakage currents, i.e., the leakage is dominantly injection-controlled.

For the crystalline films the leakage is increased (Fig. 11), and in spite of the larger scatter of the data, which is indicated by the difference for different signs of the bias at the example of the 30-nm film, there is an indication of an increase of the leakage current with increasing thickness of the films. Such a behavior has recently been observed for high-K perovskites[15–17] and discussed in relation to the low-

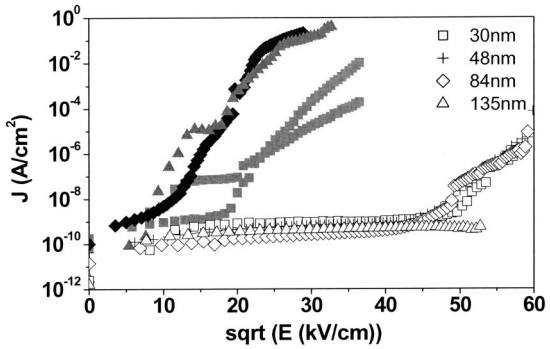

FIG. 11. Schottky plot of the leakage current for STA films on Pt electrodes. The open symbols characterize the amorphous films of different thickness and crystalline films of similar thickness are characterized by the corresponding closed symbols. The average values of the currents at positive and negative bias are shown. For the 30-nm crystalline film the differences observed with the change of the sign of the bias (Fig. 10) is shown by two different curves.

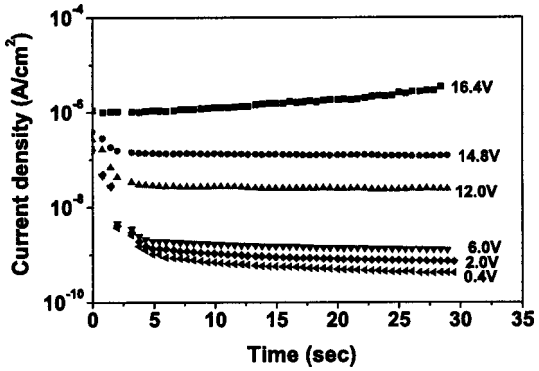

FIG. 12. Time dependence of the leakage current after a voltage step of 0.4 V for an amorphous film of 48-nm thickness. Examples are given for 0.4 V (~83 kV/cm) up to 16.4 V (~3416 kV/cm).

K interfacial layer or dead layer.[18] Hence, this behavior might be indicative of an interfacial layer for the crystalline films, which was indicated by the extrapolation of the data in Fig. 9, but could not be proven outside the error bars.

B. Pt/STA/TiN MIM capacitor structures

Due to the oxidation of the TiN electrical characterization of the films on TiN is only possible for amorphous films, as discussed above. The general C–V characteristics are similar to the films on Pt electrodes. There is, however, a slightly higher effective K value of 40 ± 5 and a significantly higher loss tangent, as shown in Fig. 13, for the range around the stoichiometric composition. The thickness dependence of the reciprocal capacity is plotted in Fig. 14 versus the film

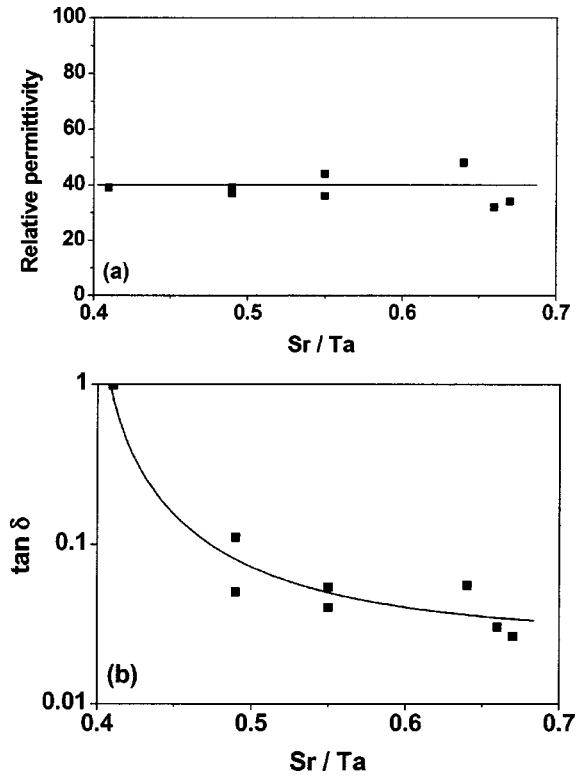

FIG. 13. Stoichiometry dependence of the relative permittivity (a) and of the loss tangent (b) for films of different stoichiometry deposited on TiN_x electrodes.

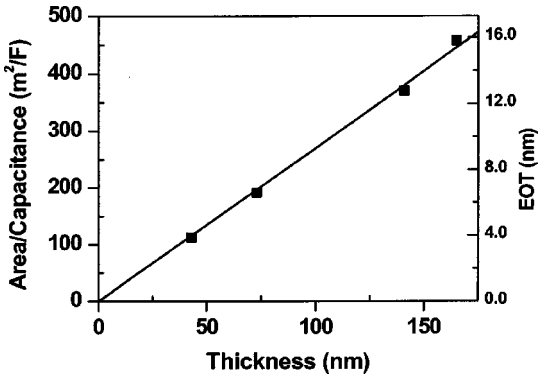

FIG. 14. Reciprocal capacity vs film thickness for Pt/STA/TiN capacitors.

thickness for films close to the stoichiometric composition. We observe a line through the origin, which indicates that there is no significant interfacial layer; consistently, the slope of the line corresponds to the effective K of 40.

With the asymmetric electrodes of the Pt/STA/TiN capacitors there is a large asymmetry in the leakage current depending on the current injection, as shown in Fig. 15. We observe currents similar to Fig. 10 for the injection from Pt electrodes and a higher current for the injection from the TiN_x, which can be attributed to the different work function. Remarkable is the better reproducibility of the data as compared to the films on Pt, and there is no systematic variation with film thickness and stoichiometry within the range of parameters shown.

C. Pt/STA/SiO$_x$/Si(100)MIS structures

The C–V behavior for amorphous STA films deposited on p-Si(l00) without removing the native oxide is shown in Fig. 16. Independent of the thickness, we observe a negative flatband voltage and a counter-clockwise hysteresis, which are related to positive oxide charges and rechargeable oxide traps, respectively. The interface trap density of the thinnest film (6 nm) used for the present study was $\sim 5 \times 10^{12}/\mathrm{eV\,cm^2}$. This film has an EOT of 2.47 nm, an average flatband voltage of about -0.7 V, a hysteresis width of ~ 0.4 V, and a leakage current density of $\sim 6 \times 10^{-4}$ A/cm^2 at -1 V. Figure. 17 summarizes the maximum capacitance obtained in the accumulation region in terms of the equivalent oxide thickness as a function of thickness. We observe a

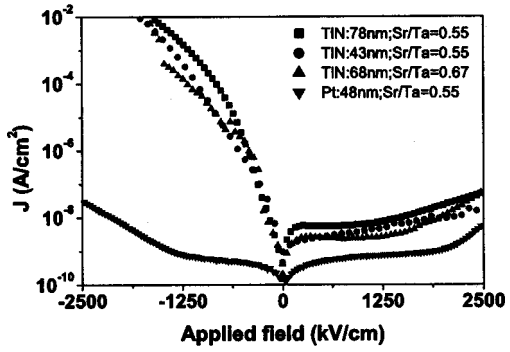

FIG. 15. Leakage current density for Pt/STA/TiN capacitors with different thickness and stoichiometry as indicated in the inset. The Pt/STA/Pt capacitor from Fig. 10 is shown for comparison.

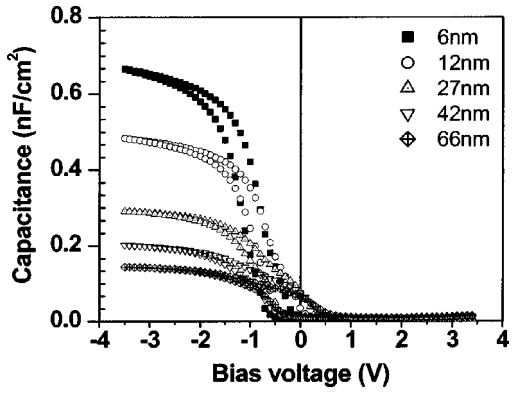

FIG. 16. C–V characteristics of Pt/STA/Si capacitors with different STA thickness.

seemingly linear behavior for the whole thickness range, however, there are systematic deviations: the thinnest films are below the extrapolated line; this might be related to the larger off-stoichiometry of these films, which had, however, no influence on the films on Pt electrodes. Therefore, the interfacial reactions are the more likely reason and the deviations from the linear behavior indicate that the interfacial layer is not stable for all films and changes slightly for longer growth times. Consequently, in applying the two-layer model to the data the intercept yields a low-ϵ SiO_x interlayer thickness of 1.5–4.2 nm, depending on the data range used for the extrapolation. Similarly, the slope yields values for the bulk-

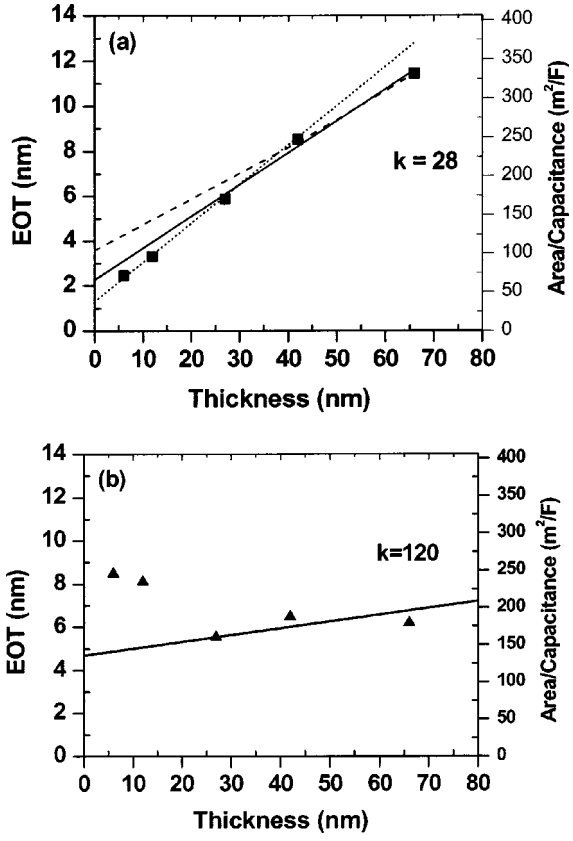

FIG. 17. Reciprocal capacity vs film thickness for Pt/STA/Si capacitors: (a) amorphous STA layers and (b) crystalline STA layers. The bold line indicates the slope for a bulk permittivity, K, as given in the figure. The dotted lines indicate the uncertainties due to the change of the slope with thickness.

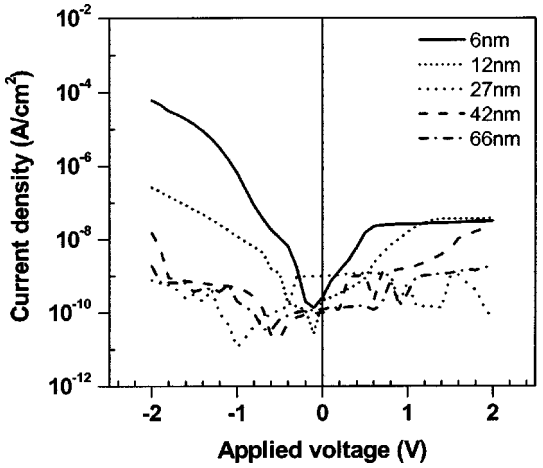

FIG. 18. Leakage current for Pt/STA/Si capacitors with different thickness.

K between 25 and 35 for considering the thinnest and thickest films, respectively. This indicates that the bulk value, as measured for the MIM structures, is reached only for rather thick films. Nevertheless, an EOT of 2.4 nm is reached for the 6-nm film. These are rather promising values considering that the interlayer may be reduced by the use of SiON.[4,5] Crystalline films show, under the given conditions, a large increase of the EOT due to interfacial reactions; this effect is larger for thin films (due to the large off-stoichiometry mentioned above, these films crystallize partly in the perovskite phase with a lower *K*), whereas for thick films the increase of the bulk *K* dominates.

Figure 18 shows the leakage current for films of different thicknesses. The leakage in accumulation is rather low, even for the thinnest film (the current density at 1 V is 10^{-6} A/cm^2 for the 6-nm film with an EOT$\sim$2.5). For thicker films the leakage current systematically decreases and for film thickness $\geqslant$27 nm the leakage current density is below 10^{-9} A/cm^2.

VI. SUMMARY AND CONCLUSION

$Sr_xTa_yO_z$ thin films with thickness between 6 and 150 nm were deposited within a wide range of Sr/Ta composition. Films were grown on $Pt/TiO_2/SiO_2/Si$, TiN_x/Si, and SiO_2/Si substrates. The as-deposited films were x-ray amorphous and could be crystallized by postannealing at temperatures $\geqslant$700 °C. The $SrTa_2O_6$ phase was dominating within a broad range of compositions (Sr/Ta: 0.4–0.7) and a perovskite-type phase was observed for Sr/Ta$>$0.8. The electrical properties were investigated for MIM and MIS applications. The amorphous films had a dielectric constant in the range of $K=35$–40 and showed very low leakage currents. No degradation was observed for films on Pt electrodes up to fields of $\sim$3 MV. The dielectric permittivity of crystalline films reached values of $K=100$–110 and was not very sensitive to deviations from the exact stoichiometry of the $SrTa_2O_6$ phase. A drastic decrease to values of $K=30$–40 is, however, observed along the phase transition at high Sr contents. In short, $Sr_xTa_yO_z$ shows very promising properties for MIM as well as MIS applications.

ACKNOWLEDGMENTS

We greatly acknowledge the help of W. Krumpen, who carefully performed the XRF analysis, and of H. Haselier, who deposited the Pt electrodes. We thank Dr. P. Lehnen, S. Miedl, and Dr. M. Schumacher from AIXTRON AG for useful discussions.

[1] A. I. Kingon, J. P. Maria, and S. K. Streiffer, Nature (London) **406**, 1032 (2000).
[2] D. G. Schlom, C. A. Billman, J. H. Haeni, J. Lettieri, P. H. Tan, R. R. M. Held, S. Völk, and K. J. Hubbard, Appl. Phys. A: Mater. Sci. Process. (in press).
[3] W. J. Lee, I.-K. You, S.-O. Ruy, B.-G. Yu, K.-I. Cho, S.-G. Yoon, and C.-S. Lee, Jpn. J. Appl. Phys., Part 1 **40**, 6941 (2001).
[4] M. A. Rodriguez, T. J. Boyle, B. A. Hernandez, D. R. Talland, and K. Vanheusden, J. Am. Ceram. Soc. **82**, 2001 (1999).
[5] E. Tokumitsu, G. Fujii, and H. Ishiwari, Appl. Phys. Lett. **75**, 575 (1999).
[6] D.-O. Lee *et al.*, Microelectron. Eng. **59**, 405 (2001).
[7] M. J. Crosbie, P. J. Wright, H. O. Davis, A. C. Jones, T. J. Leedham, P. O'Brien, and G. W. Critchlow, Chem. Vap. Deposition **5**, 9 (1999).
[8] S. Regnery, R. Thomas, H. Haselier, P. Ehrhart, R. Waser, P. Lehnen, S. Miedl, and M. Schumacher, Mater. Res. Soc. Symp. Proc. **811**, D9.7.l (2004).
[9] B.-G. Chae, W.-J. Lee, I.-K. You, S.-O. Ryu, M.-Y. Jung, and B.-G. Yu, Jpn. J. Appl. Phys., Part 2 **41**, L729 (2002).
[10] W. J. Lee *et al.*, Integr. Ferroelectr. **46**, 275 (2002).
[11] P. Ehrhart *et al.*, Integr. Ferroelectr. **30**, 183 (2000).
[12] B. Lengeler, in *Photoemission and Absorption Spectroscopy with Synchrotron Radiation*, edited by M. Campagna and R. Rosei (North-Holland, Amsterdan, 1990), p. 157.
[13] A. R. Teren, R. Thomas, J.-Q. He, and P. Ehrhart, Thin Solid Films **478**, 206 (2005).
[14] International Centre for Diffraction Data, ICDD, powder diffraction files.
[15] Y. C. Shin, J. Park, C. S. Hwang, and H. J. Kim, J. Appl. Phys. **86**, 506 (1999).
[16] F. Fitsilis, S. Regnery, P. Ehrhart, R. Waser, F. Schienle, M. Schumacher, and H. Juergensen, Integr. Ferroelectr. **38**, 211 (2001).
[17] S. Regnery *et al.*, Mater. Res. Soc. Symp. Proc. **748**, U15.6.1 (2003).
[18] H. Schroeder and S. Schmitz, Appl. Phys. Lett. **83**, 4381 (2003).